Eur. Phys. J. Plus (2025) 140:59
https://doi.org/10.1140/epjp/s13360-025-05988-9

THE EUROPEAN PHYSICAL JOURNAL PLUS

Regular Article

Micro-computed tomography and laser micro-ablation on altered pyrite in lapis lazuli to enhance provenance investigation: a new methodology and its application to archaeological cases

Marta Magalini[1,2], Laura Guidorzi[1,2,a], Alessandro Re[1,2], Francesca Tansella[1,2], Federico Picollo[1,2], Sofia Sturari[1,2], Pietro Aprà[2], Georgina Herrmann[3], Randall Law[4], Quentin Lemasson[5,6], Laurent Pichon[5,6], Brice Moignard[5,6], Claire Pacheco[5,6], Alessandro Lo Giudice[1,2]

[1] Dipartimento di Fisica, Università di Torino, Via Pietro Giuria 1, Turin, Italy
[2] INFN Sezione di Torino, Via Pietro Giuria 1, Turin, Italy
[3] University College London (UCL), Gower Street, London WC1E 6BT, UK
[4] Department of Anthropology, University of Wisconsin, 5240 Sewell Social Sciences Building, 1180 Observatory Drive, Madison, USA
[5] Centre de Recherche et de Restauration des Musées de France, C2RMF, 14 quai François Mitterrand, Paris, France
[6] UAR 3506 Lab-BC (CNRS, Ministère de la Culture, Chimie ParisTech), 14 quai François Mitterrand, Paris, France

Received: 27 September 2024 / Accepted: 4 January 2025

Abstract This work presents an upgrade to the methodology adopted to investigate the provenance of the raw lapis lazuli material used in antiquity for carving precious artefacts. Samples from archaeological excavation contexts frequently display superficial degradation processes affecting the crystals of the mineral phases useful for provenance attribution (especially pyrite). To address this issue, an innovative workflow has been developed, centred on the application of X-ray micro-computed tomography (μ-CT) and micro-ablation treatments with a pulsed laser source prior to investigation with ion beam analysis (IBA). High-resolution μ-CT is employed to evaluate the alteration state of pyrite crystals within the entire volume of the lapis lazuli rock, and, if required, to identify the most suitable crystals on the surface for subsequent laser treatment. The micro-ablation procedure aims to create a small breach in the superficial altered layer (the irradiated areas are approximately $65 \times 65\ \mu m^2$), thereby exposing the preserved crystal beneath and allowing for the analysis of its trace element contents with IBA. The methodology of the workflow is presented, together with its first application to archaeological lapis lazuli material: three precious beads from the ancient Royal Cemetery of Ur (Mesopotamia, 3rd millennium BCE). The results are complemented by the application of a provenance protocol already validated that proved, for the first time using a micro-invasive analytical approach, a match between the Afghan quarry district and the raw material used to carve these beads.

1 Introduction

Lapis lazuli is a semi-precious stone that has been used since the 5th millennium BCE for the carving of valuable items and decorative objects, including jewels, amulets, statuettes and inlays. Archaeological findings made by this rock have been discovered in a vast territory, from the ancient Middle East and Egypt to Central Asia, especially in sites of the 3rd millennium BCE, when the greatest popularity of this material occurred. Regarding the sources of the rock, due to the very restricted geological environment necessary for its formation, there are only few sites on Earth where lapis lazuli can be extracted. Although the Badakhshan quarries in Afghanistan are widely considered to be the only sources of lapis lazuli in ancient times, others have been cited or suggested [1–5]. Obtaining information on the provenance of the raw material of archaeological artefacts could, therefore, provide very interesting indications on the most active mining areas at a given time, the distances travelled to trade this material and, indirectly, the socio-economic links between the populations that traded it.

Investigating the lapis lazuli provenance is a complex challenge due to the high heterogeneity of this rock, which consists of an aggregate of different minerals (more than 30 phases in lapis lazuli have been documented in the literature [6, 7]). The most characteristic mineral is lazurite, an alumino-silicate of the complex feldspathoid sodalite group, which confers the typical blue colour that has fascinated many populations throughout antiquity. Additionally, minerals, such as pyrite, diopside, phlogopite, calcite, K-feldspar and numerous others, can occur with varying abundances. The characterisation of the compositional and luminescence properties of some of these mineral phases (in particular, diopside, wollastonite and pyrite) with ion beam analysis (IBA) has demonstrated to be an effective method for differentiating rocks from different extraction sites [8, 9]. The same procedure is being

[a] e-mail: laura.guidorzi@unito.it (corresponding author)

Published online: 22 January 2025

extended to the study of calcite, and results will be published soon. In these studies, an analytical approach based on the investigation of a large set of reference rocks with μ-particle-induced X-ray emission (μ-PIXE) and μ-ion beam-induced luminescence (μ-IBIL) techniques was developed. The reference materials were sourced from five distinct geographical regions: Afghanistan, Tajikistan, Siberia, Myanmar and Chile. IBA allows to investigate micrometric single crystals of the phases of interest, ensuring a non-invasive approach, which is often essential when dealing with precious artefacts. In the analytical protocol presented in [9], the provenance discrimination is based on the identification of a series of markers, such as the presence of specific trace elements in certain quantities or the appearance of characteristic bands in the luminescence spectra.

However, the evaluation of these markers is only possible when the crystal under analysis is well preserved, as alteration processes or external contamination could modify the stoichiometry of the mineral, leading to high scattering of data on trace element concentrations or, in extreme cases, to the impossibility of the analysis itself. This phenomenon especially occurs in archaeological materials that have been buried for centuries in conditions of high humidity, percolating waters or thermal stress, which can lead to the degradation of the surface layer. In [10], an analysis of different weathering processes affecting lapis lazuli archaeological materials is discussed. Among the various mineral phases present in lapis lazuli, pyrite (FeS_2) appears to be particularly susceptible to modification under these unfavourable conditions. Pyrite partially transforms into iron oxide–hydroxide minerals (e.g. hematite, goethite and jarosite) from the surface or fractures towards the inner part of the crystal via a sequence of complex oxidation reactions [11]. These processes result in the formation of brown- or red-stained grains, which are unsuitable for a reliable quantitative analysis with μ-PIXE and, consequently, for the extraction of useful provenance information. Indeed, the analysis of unaltered pyrite crystals has demonstrated that the evaluation of the Cu-Ni ratio allows for the clear distinction between Tajik and Afghan rocks [12]. This ratio is considered a strong marker, that is, according to the definition given in [9], a physical–chemical characteristic that is systematically present or absent in all the analysed samples from a specific provenance.

In order to address the issue of altered pyrite, an innovative workflow in the context of lapis lazuli investigation has been developed, and it is illustrated in this paper. It comprises three phases: a characterisation phase, during which X-ray micro-computed tomography (μ-CT) is performed on the object under analysis to verify the presence of pyrite crystals with a pristine core and to select the largest ones that emerge on the surface; an in-air micro-ablation treatment by means of a micro-pulsed laser source strictly targeting the superficial alteration of the selected crystals and, finally, the analysis of the treated areas with IBA. The core of the procedure is the micro-ablation, which aims to create a small breach in the alteration layer of the pyrite, thereby allowing the proton beam used in subsequent IBA to reach the preserved crystal beneath. The utilisation of laser ablation on extended surfaces in cultural heritage materials (e.g. stones, metals, paintings and paper) is nowadays a well-established conservation cleaning treatment [13, 14]. Conversely, its application to micro-scale areas is considerably less prevalent in this field. The feasibility of laser micro-cleaning has been demonstrated previously by [15] in the study of corrosion layers on metal artefacts, but, to the best of our knowledge, this technique has never been applied to lapis lazuli material.

Together with the methodology of the new workflow, this study presents its first application to lapis lazuli archaeological material. In particular, three lapis lazuli beads from the ancient Royal Cemetery of Ur (modern Iraq, 3rd millennium BCE) were analysed. The city of Ur was one of the highest consumers of lapis lazuli in South Mesopotamian markets during the 3rd millennium, and many different items made or decorated with lapis lazuli inlays have been found in the royal tombs of its cemetery (e.g. jewellery, statuettes and boxes) [16]. More details about the samples analysed in this work and their archaeological context are given in Sect. 3. In addition to the results from the laser-treated pyrite crystals in the Ur beads, the outcomes of the IBA analysis of diopside crystals will also be presented. Following the provenance protocol outlined in [9], this study will attempt to assess the geological origin of the raw material used in the production of these beads, and to demonstrate, for the first time through micro-invasive physical–chemical analysis, the potential Afghan provenance of the lapis lazuli material found in Ur, as hypothesised by archaeologists.

2 Instruments and analytical methods

The ultimate goal of the proposed workflow is to enhance the characterisation of pyrite crystals in a lapis lazuli sample. The procedure aims to be applicable to precious lapis lazuli artworks, so all the techniques employed were selected to be as minimally invasive as possible. The procedure can be applied directly to artefacts without the need for any significative invasive pre-treatment, such as cutting or carbon coating. With regard to the dimensions of the objects that can be analysed, the main constraints arise from the volume of the chamber of the laser instrument and the focal plane distance associated with the selected optics. The instrumentation available in this work allows for the potential treatment of objects with dimensions of up to 7×7 cm^2 in the plane orthogonal to the laser beam and up to 2 cm in the direction parallel to the beam.

The three steps of the workflow are presented in the following:

(1) *Characterisation with μ-computed tomography.* X-ray computed tomography has become an invaluable tool in the context of cultural heritage study, thanks to its non-invasive capability to visualise the inner part of an object and its high flexibility in terms of analysable material [17]. Nevertheless, the specific use of μ-CT to potentially identify the distribution of different mineral phases forming a rock remains a significant challenge due to the considerable complexity of the material and the necessity for phase compositions and densities to differ sufficiently to yield discernible differences in X-ray attenuation. Some examples of

applications to geomaterials are discussed in [18, 19]. In the case of the lapis lazuli material, in this work, we demonstrated that a high-resolution X-ray micro-tomography is an effective method for identifying the location of pyrite crystals within the analysed sample, as well as for assessing their alteration status, exploiting the difference in their absorbing rate. Since the thickness of the alteration layer could be of the order of a few tens of micrometres, a high spatial resolution is necessary in the reconstructed volume. When investigating the provenance of lapis lazuli artefacts, this characterisation step can be employed to confirm or exclude the Siberian origin, as only rocks from Siberia, among those in our dataset [8], have pyrite crystals in a fully altered state. This phenomenon occurs even in the innermost parts of the volume, as the alteration process takes place during the formation of the rock. The μ-CT can be further utilised to select the largest pyrites with a pristine core and superficially visible, which can then be subjected to the subsequent step of the workflow.

(2) *Laser micro-ablation.* This procedure aims to expose the target altered pyrites to the laser until the pristine crystal is reached. In order to remain as minimal invasive as possible, the dimensions of the irradiated areas on pyrite were selected to be $65 \times 65\ \mu m^2$, this value considers the typical dimension of an in-air proton beam (about 30–40 μm), also used in this work, and guarantees that the surrounding areas of the sample are not affected by the laser treatment. We demonstrated that by using a green (532 nm) pulsed laser (pulses duration 6 ns) at an energy per pulse of 0.6 mJ, it is possible to remove the alteration on pyrite. During the micro-ablation of a sample, two guidelines are of assistance to the user in stopping the irradiation process: the value of alteration depth known from the μ-CT and the change in the reflectance of the area when the pristine core is reached during ablation, which is visible using a microscope, if incorporated in the laser system. At the end of the process, the treated areas are not easily distinguishable at naked eye. Scanning electron microscopy coupled with microanalysis (SEM–EDX) in variable pressure can provide additional validation of the reaching of the pristine pyrite. By acquiring elemental maps of the treated area, the appearance of sulphur and the corresponding disappearance of oxygen and other contaminating elements confirms the success of the ablation treatment.

3) *Ion beam analysis.* Once the pristine core of a pyrite crystal is exposed, μ-PIXE measurements can be performed to investigate its composition, looking for provenance markers in the trace elements, in particular Ni and Cu concentration values. As explained in [9], if a pyrite meets the $Cu < 0.6 \cdot Ni$ condition, the Tajik provenance can be excluded; conversely, the Afghan origin can be discarded. In the case of precious artefacts, an in-air beam is mandatory as it guarantees non-invasive measurements and great flexibility in sample placement (the investigated area should be as orthogonal as possible to the beam direction).

A series of tests were conducted to assess the best working conditions for the first two steps of the workflow. Regarding μ-CT, an initial test was done on a not precious lapis lazuli sample containing altered pyrites in order to verify the capability of the μ-CT to distinguish between altered and not altered areas in a pyrite. The test sample was prepared as a cross-section (about 400 μm thickness) by embedding it in epoxy resin and cut to expose its inner part. This allowed to compare the μ-CT image of a partially altered pyrite in the section with the corresponding optical image and electron backscattered image acquired with a scanning electron microscope (SEM-BSE). The results of this test are discussed in Sect. 4.1. The μ-CT scan was obtained with the instrumentation available at the Physics Department of the University of Torino, a custom and versatile instrument that has already shown its potentiality on beads with similar dimension but different materials (pearls [20], shells [21] and glasses [22]). For this application, the home-made instrument is equipped with a Hamamatsu Microfocus L8121-03 X-ray source, a Newport URS150BPP rotation stage and a Teledyne Dalsa Shad-o-Box 6 K HS flat panel detector (2304×2940 pixels, pixel size 49.5 μm, active area $11.4 \times 14.6\ cm^2$). The X-ray source has a focal spot size of 7 μm. For the acquisition, the voltage and the current were set to 150 kV and 66 μA, respectively. A total of 2400 projections were acquired during the tomography, with an angular step of 0.15° and an integration time of 1.9 s for each radiography, leading to an average time of 150 min for a CT scan. The source–detector distance (SDD) and the object–detector distance (ODD) were set to 650 mm and 560 mm, respectively. The final voxel dimension obtained was 7 μm. Figure 1a shows the μ-CT apparatus in the same measurement condition during the acquisition of one of the beads from Ur, performed as a first application of the workflow to an archaeological case study. Several software packages were utilised for CT reconstruction and visualisation: ParRec [23] for flat-field correction and CT reconstruction, ImageJ [24] for the visualisation and basic handling of the image sequences and Dragonfly (version 2022.1, ORS Inc., Montréal, QC, Canada) and VGStudio Max (version 2.2, Volume Graphics GmbH, Heidelberg, Germany) for the 3D rendering of CT volumes, segmentations and dimensional measurements.

Regarding the second step of the workflow, the laser micro-ablation treatment, several tests were conducted on a partially altered pyrite within another lapis lazuli sample prepared as a cross-section. These tests aimed to determine the optimal laser wavelength (either 1064 nm or 532 nm) and energy per pulse. An EzLaze Nd:YAG 3 ns-pulsed laser source normally used in semiconductor industry for silicon wafer marking was employed for the localised micro-ablation procedure at the Physics Department of the University of Torino. The laser emits in the IR (1064 nm), VIS (532 nm) and UV (355 nm) wavelengths. The pulses duration is 6 ns, and the nominal maximum energy per pulse is 0.6 mJ, with an instant power of 100 kW. The energy per pulse ranges from 0 to 0.6 mJ, and specific tests were conducted at 0.6 mJ and 0.2 mJ. The results of the test are discussed in Sect. 4.1. Through a series of dedicated high-power compatible optics and variable collimation apertures, the laser beam can be focused on different scale areas. Using a 20 × objective, it possible to irradiate an area of $65 \times 65\ \mu m^2$. The SEM–EDX instrumentation used in this work to check the success of the treatment is a Zeiss EVO 60 scanning electron microscope equipped with a LaB_6 filament and a Bruker Quantax

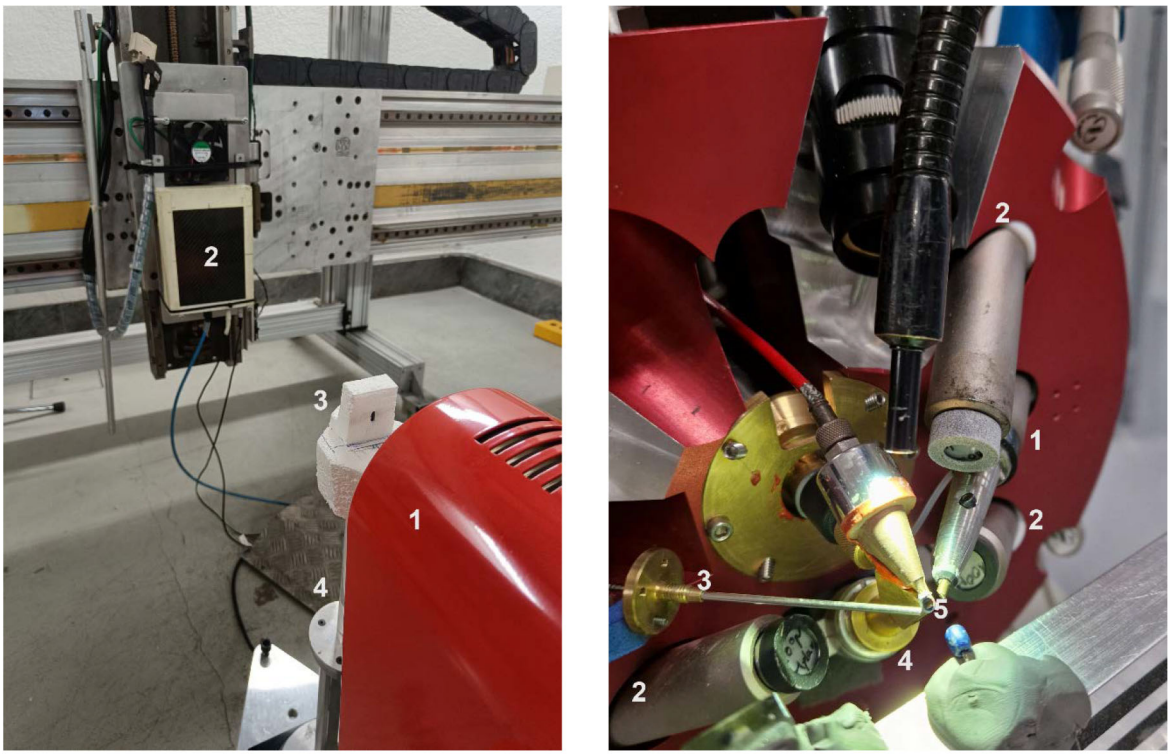

Fig. 1 **a** μ-Computed tomography apparatus at the Physics Department of the University of Torino. 1 = microfocus X-ray source, 2 = X-ray flat panel detector, 3 = polystyrene support holding one of the Ur beads at the centre and 4 = rotating stage. **b** The external microprobe of the New AGLAE facility (C2RMF, France) during Ur bead analysis. 1 = Low-energy SDD detector, 2 = high-energy SDD detectors, 3 = optical fibre and 4 = SDD dose detector, from which the deposited charge is monitored. 5 = Si_3N_4 exit window. More details in [25]

200 EDX microprobe, working at variable pressure (50 Pa) and with a voltage set at 20 kV. The instrument is hosted in the scientific laboratories of the Centro Conservazione e Restauro "La Venaria Reale" in Venaria Reale, Torino (Italy).

Adopting the best analytical conditions found after the tests phase, the workflow was applied for the analysis of precious archaeological items: three lapis lazuli beads from Ur (described in Sect. 3). Three or four superficially altered pyrite crystals in each bead, for a total of 10 crystals, were selected exploiting μ-CT and treated with the laser micro-ablation. These pyrites were then analysed with IBA at the New AGLAE accelerator facility; three altered crystals not treated were also acquired for comparison. At the New AGLAE facility (C2RMF, Paris, France) [25, 26], a 3 MeV in-air proton beam with a diameter of 30–40 μm is available. The μ-PIXE set-up consists of four SDD detectors (KETEK AXAS-M): one detector is dedicated to the measurement of low-energy (LE) X-rays (1–10 keV), and it is fluxed with helium gas to improve its detection efficiency; the other three SDD detectors, screened with 100 μm Mylar absorbers, are dedicated to measure high-energy (HE) X-rays (>3 keV). The deposited charge is monitored by recording Si X-rays emitted by the Si_3N_4 100 nm thick beam exit window by means of a dedicated SDD detector. When luminescent mineral phases are analysed (e.g. diopside), μ-IBIL can be simultaneously performed. The set-up consists in a 1 mm diameter optical fibre placed at 45° angle with respect to the beam direction. It collects the light and leads it to an Ocean Optics QE65000 spectrometer recording from 200 to 1000 nm with a resolution of 3 nm (using a 100 μm entrance slit). Figure 1b shows the endpoint set-up of the ion micro-beam line during the analysis of one of the beads from Ur. Large 2D PIXE and IBIL maps (e.g. 500 × 500 μm^2) can be scanned by the beam around the crystal under analysis; the sub-areas of interest are then selected pixel by pixel (pixel dimension 25 × 25 μm^2) during post-acquisition data processing, using the custom-made software AGLAEMap [27]. A set of reference mineral standards (SPI #02753-AB Mineral Standards) is employed for calibration. μ-PIXE data are processed with the custom-made software TRAUPIXE [27], whereas all the μ-IBIL spectra are corrected in intensity for the instrumental efficiency at different wavelengths. The results of pyrite investigation in the Ur beads are presented in Sect. 4.2.1.

To complete the provenance investigation following the protocol described in [9], diopside mineral phase was also analysed in the Ur beads. Differently from pyrite, diopside crystals were found in good conservation state. The beads were firstly pre-characterised with cold-cathodoluminescence (cold-CL) microscopic imaging for the identification and mapping of the different mineral phases present. The instrument employed was a CITL cold cathode luminescence 8200 mk3 instrument equipped with a polarised optical microscope Olympus BH2 and a Peltier-cooled Olympus DP74 camera, hosted at the Earth Science Department of the University of Torino. The accelerating voltage and current employed were 15 kV and 500 μA, respectively. For each bead, a total of about 10

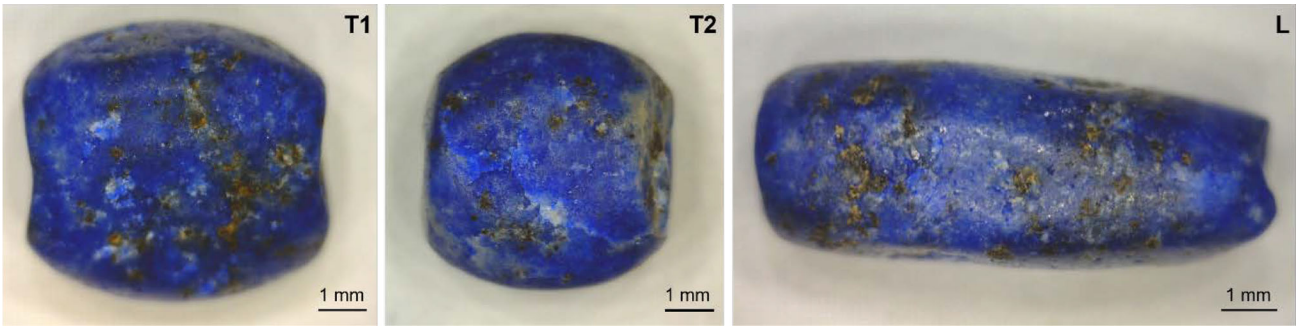

Fig. 2 Optical microscopy images of the three lapis lazuli beads from Ur (Mesopotamia, 3rd millennium BCE)

images per side were acquired (magnification × 2.5, exposure time 50 ms for each image) and later stitched together with the Adobe Photoshop software (version 22.0.1). A rapid survey of the samples was then conducted with SEM–EDX in variable pressure to assess the largest, most homogeneous and well-preserved diopside crystals. Finally, a total of 25 crystals were analysed together with pyrites with μ-PIXE and μ-IBIL at the New AGLAE facility. The results of diopside investigation in the Ur beads are presented in Sect. 4.2.2.

3 The archaeological samples

Two great archaeological discoveries were made in the 1920s: the Royal Graves at Ur of the Chaldees, the city of Abraham, in southern Mesopotamia (Iraq), by Leonard Woolley, and the tomb of the young Pharaoh, Tutankhamun, in the Valley of the Kings in Egypt, by Howard Carter. Unimaginable quantities of treasure were found in both. Although it had been assumed for over a century that the vast quantities of lapis lazuli found in both had been brought from a single source in far distant Badakhshan in North–east Afghanistan, it could not be proven by means of analytical techniques. Recent applications of physico-chemical analysis are trying to solve these archaeological questions, focusing in particular on the materials from Ur. The Royal Graves of Ur were extensively excavated by the joint expedition of the British Museum and the Museum of the University of Pennsylvania, under the direction of Sir Leonard Woolley [16]. He found more than 1800 graves and tombs, which were lavishly equipped with objects made of gold, lapis lazuli and carnelian. The quantity and variety of objects made of, or decorated with, lapis lazuli represent one of the greatest examples of the use of this material. A summary of the most relevant objects discovered by Woolley includes amulets, statuettes, dagger handles, vases and jewellery, as well as elaborate inlays on lyre boxes and gaming boards, etc. [2].

A preliminary study on the provenance of lapis lazuli used to carve two beads found in Ur and based on sulphur isotope analysis was conducted by R. Law using the same methodology described in [28]. The results are presented in Online Resource 1, they show for the first time a compatibility with a set of reference rocks from Badakhshan and an incompatibility with reference rocks from Siberia and Myanmar. However, the method adopted in Law's study is destructive and, therefore, very prohibitive for extended applications to valuable archaeological artefacts. In this work, the provenance of three other lapis lazuli beads (Fig. 2), labelled as T1, T2 and L, found in a Royal Grave from the 3rd millennium BCE at Ur was investigated with micro-invasive techniques, as described in Sect. 2. Concerning their conservation status, the beads present heavily altered pyrites visible on the surface. Instead of their typical gold-like colour, the crystals appear in brownish or reddish grains. Figure 3 shows a series of examples of altered pyrites for each bead.

4 Results and discussion

4.1 μ-Computed tomography and laser micro-ablation test

The outcome of the test about the capacity of μ-CT to visualise pyrite crystals and their alteration within lapis lazuli is illustrated in Fig. 4. The figure shows the comparison between the optical microscopy, the SEM-BSE image and the corresponding μ-CT slice of a partially altered pyrite in a cut lapis lazuli test sample. The unaltered pyrite (gold-like areas in the optical image) corresponds to the brighter regions observed in both the SEM-BSE image and the μ-CT slice (it can be seen that the crystal shape differs slightly in the two images, due to the difference in the depth of the virtual cut made for μ-CT and the penetration depth of the electron beam). Indeed, due to the higher X-rays absorption of pyrite in comparison with all the other mineral phases within the lapis lazuli sample, it is possible to easily map the presence of this phase in the volume and to exploit the dimensional information provided by μ-CT to measure the crystal size. As expected, the spatial resolution of the μ-CT image is worse with respect to the SEM-BSE image. However, it is still adequate for visualising the alteration that develops along the cracks of the crystal, which appears as a

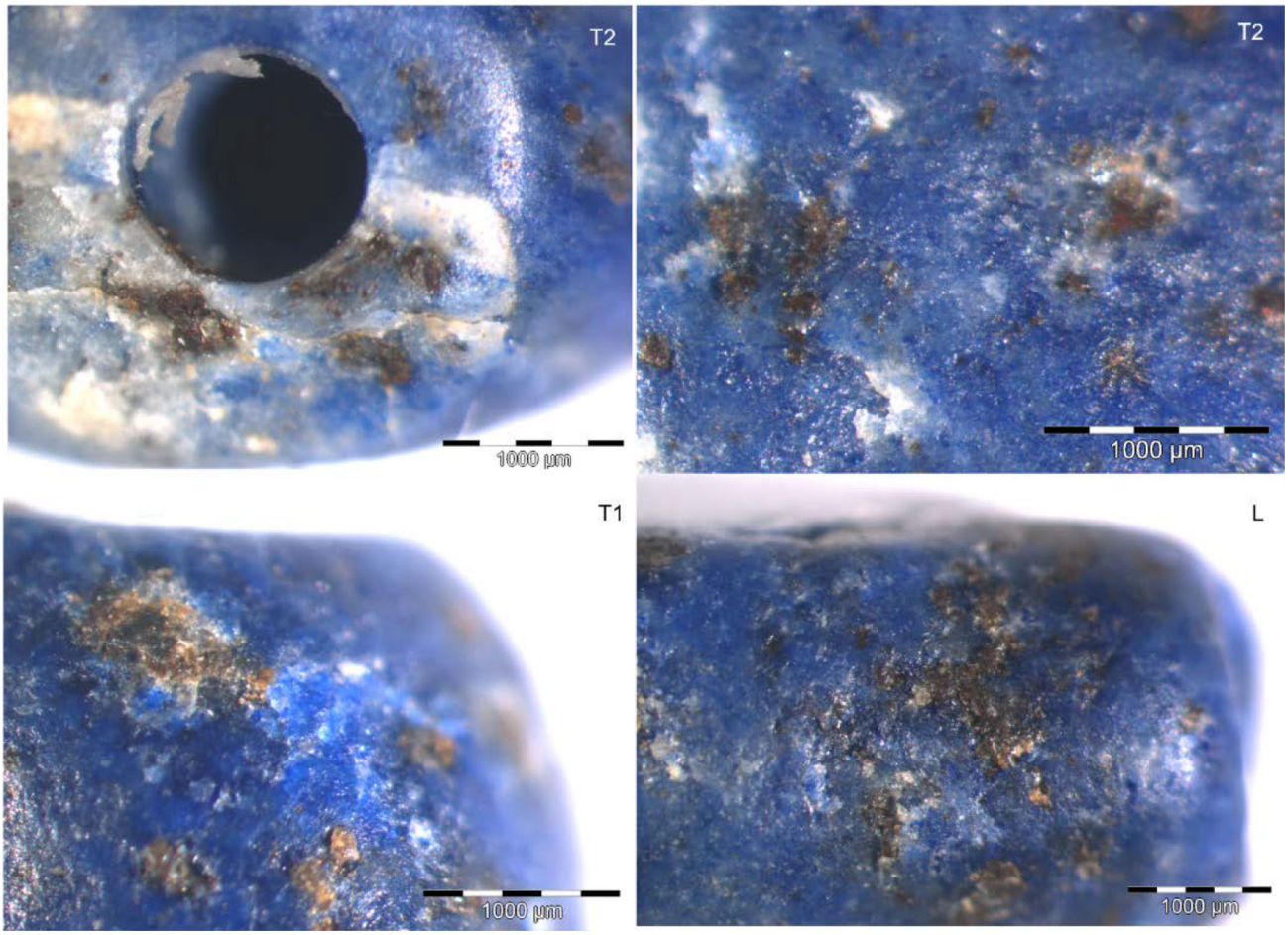

Fig. 3 Optical microscopy images of the Ur beads where pyrite crystals with alterations of different colour shades (from brown to red) are visible

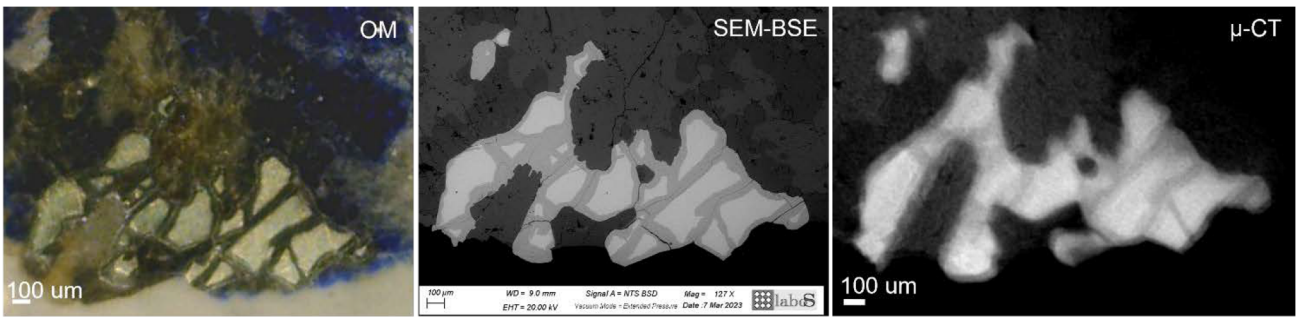

Fig. 4 Comparison of the images of the section of a partially altered pyrite in a cut lapis lazuli test sample (the weathering exposed surface was at the bottom) obtained, from left to right, by optical microscopy, SEM-BSE and µ-CT

darker grey level in comparison with the pristine pyrite. This is due to the different radiopacity resulting from the loss of S and the remaining of Fe and O as main elements in the alteration. Given the good analytical power of these tomographic results, the same experimental conditions can be used for the investigation of precious lapis lazuli artefacts.

Regarding the optimisation of the laser micro-ablation parameters, Fig. 5 shows the hit areas in the second test sample, while Table 1 reports the indication of the wavelength, the energy per pulse and the total number of pulses set for each area. It is interesting to observe that infrared laser at 1064 nm has practically no effects on the alteration layer, whereas it modifies the pristine pyrite (see area 1 in Fig. 5). Green laser (532 nm) instead is able to ablate both type of areas, producing a greater excavation depth in the unaltered pyrite than in the altered part (see, for example, areas 5–6 in Fig. 5). This observation suggests that the laser ablation process for this material is not constrained by self-limiting effects, whereby the laser wavelength is strongly absorbed by the superficial crust but reflected by the substrate. Consequently, meticulous attention is needed during the removal of the alteration layer. In the final

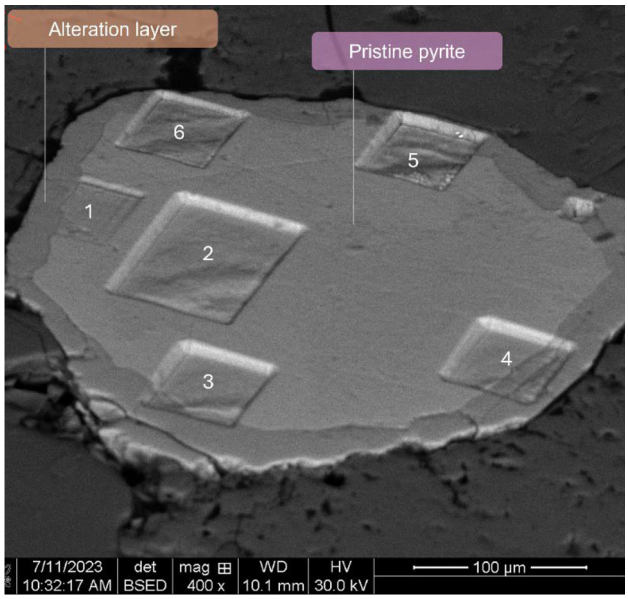

Fig. 5 Test pyrite used to determine the best working condition for the micro-laser ablation. The parameters used for each area are reported in Table 1

Table 1 Laser parameters for each irradiated area: wavelength (IR = 1064 nm, VIS = 532 nm), energy per pulse and number of pulses

Area	Wavelength	Energy per pulse	N° of pulses
1	IR	0.6 mJ	20
2–3-4	VIS	0.6 mJ	20
5	VIS	0.2 mJ	30
6	VIS	0.2 mJ	20

operating parameters, the maximum energy per pulse available was selected, as pulses with lower energy produced no discernible differences in the irradiated area, but only a lower digging depth (compare, for example, areas 3 and 6 in Fig. 5). With the selected conditions, we estimated that 90 green (532 nm) laser pulses at 0.6 mJ energy per pulse can remove about 20 µm of alteration layer, the typical thickness of altered pyrites found in the archaeological samples from Ur and measured from the micro-CT reconstructed slices.

4.2 Provenance investigation of Ur beads

4.2.1 Pyrite analysis

The results of the application of the new workflow for the characterisation and the treatment of altered pyrites in the Ur beads will be firstly discussed, followed by the analysis of diopside crystals and the implication for the provenance study.

The high-resolution µ-CT acquired on the three beads allowed to easily map the pyrite crystals present in each sample and obtain an estimate of their 3D dimension. Figure 6 shows a representative example of the appearance of a reconstructed tomographic volume of a lapis lazuli bead and the corresponding optical image (upper left corner). In the figure, one of the selected pyrites is indicated with a green arrow, and it is displayed in three tomographic slices in the horizontal (*xy*), axial (*xz*) and longitudinal (*yz*) planes. Additionally, the subfigure in the *xz* plane illustrates the measurement of the main dimensions of the pyrite. With regard to the alteration state evaluation, the tomographic slices allowed the straightforward assessment that the pyrites of the Ur beads presented an unaltered core in their inner part and an alteration that developed along the edges of the crystals, which could be distinguished by their different greyscale values (as explained in Sect. 4.1). These features were highlighted through the segmentation of the alteration layer (depicted in red colour in the example in Fig. 6 (*xz*, *yz*, *xy* planes)) by selecting a suitable range of greyscale values. The segmentation process occasionally struggles to detect the inner altered fractures, probably due to their small size relative to the voxel dimension. However, this approach can still be very useful to derive an estimate of the superficial crust that need to be removed through the laser micro-ablation. Pyrites with the largest dimensions, a pristine core and accessible from the surface were selected for the subsequent laser micro-ablation treatment, for a total of 3 pyrites in T1 bead, 4 in T2 bead and 3 in L bead.

In each of the selected pyrite, one squared area (or more than one when possible) was hit with about 90 laser pulses at 532 nm under the conditions described in Sect. 4.1. The confirmation of the successful micro-ablation to reach the pristine core was obtained subsequently from SEM–EDX elemental mapping of the irradiated areas. Figure 7 shows an example of three ablated zones in a pyrite of T2 bead. In Fig. 7a, the BSE image of the entire area is visible (top) along with a zoom on the two cleaned squares in

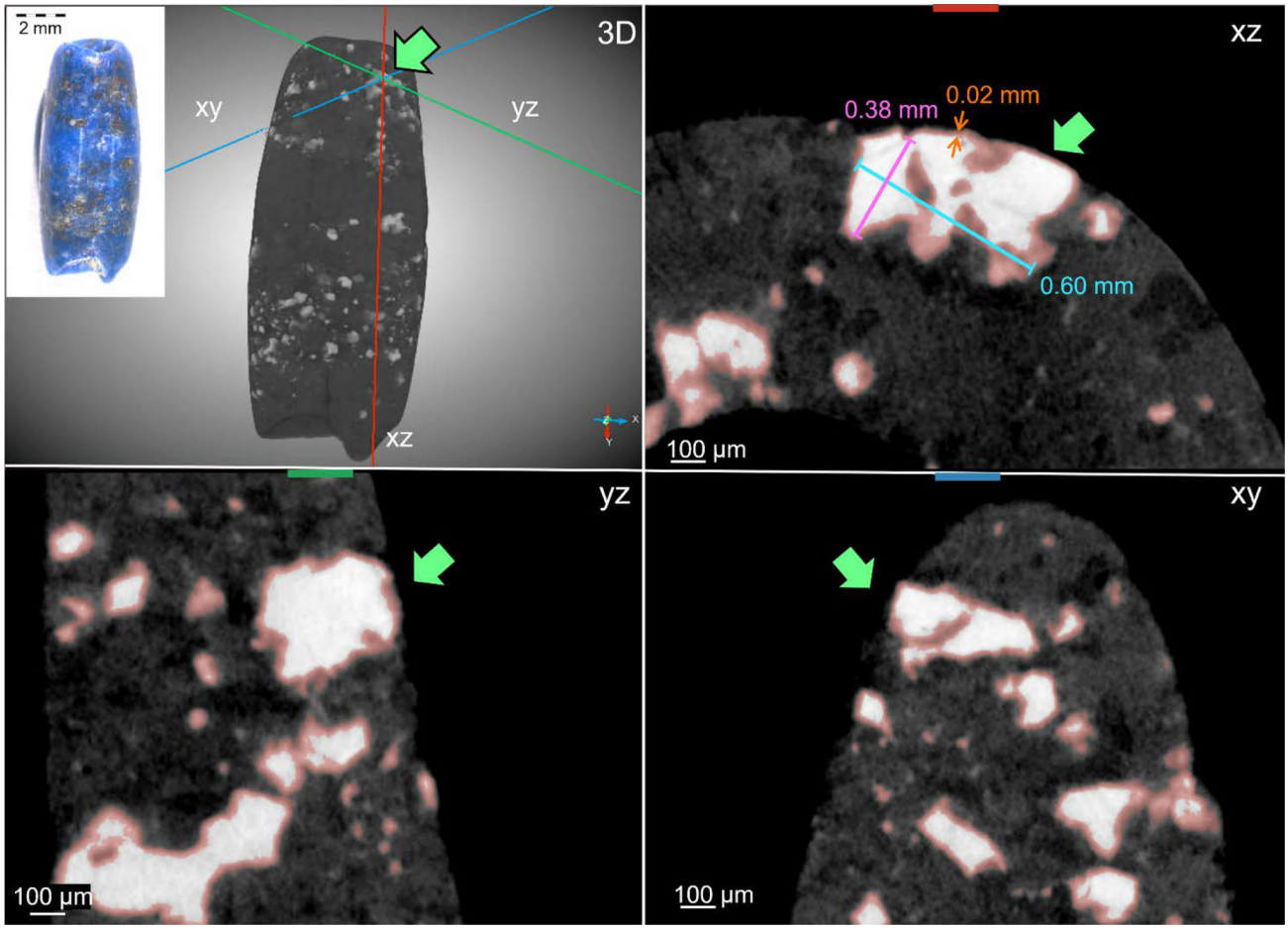

Fig. 6 Micro-CT reconstructed 3D volume of L bead and the corresponding optical image (upper left). CT horizontal (*xy*), axial (*xz*) and longitudinal (*yz*) slices of a partially altered pyrite (pointed by a green arrow) accessible from the surface of the bead. The alteration layer is highlighted in red colour by a grey-level threshold segmentation procedure. The measurements of the main size the crystals and of its alteration layer are also reported in the *xz* plane

the lower part of pyrite (bottom). In Fig. 7b, the corresponding elemental maps of the major elements are shown. The distribution of elements changes in the micro-cleaned areas. Sulphur emerges clearly, while oxygen, silicon and calcium that were part of the alteration layer are largely removed, remaining instead well-visible in the surrounding area.

When analysing pyrite crystals with IBA at the New AGLAE facility, analogous compositional maps can be obtained with μ-PIXE, but with some relevant differences due to the characteristics of the technique. For example, oxygen is not detectable with μ-PIXE, whereas trace elements such as Ni and Cu can be mapped. The spatial resolution of the maps is lower due to the larger size of the proton beam compared to the electron beam in SEM–EDX; moreover, the penetration depth of the two probes also differs considerably, contributing to the potential discrepancy in the observed elemental distributions. However, it is still quite easy to identify the areas of interest from the correspondence between the sulphur and iron maps, as visible in the example in Fig. 8, which shows the same area as Fig. 7a. In the bottom part of Fig. 8a, the overlay of the SEM-BSE image with the elemental map of S (rotated and scaled accordingly) is shown; the correspondence between the micro-clean areas and the appearance of S is clearly visible. In the μ-PIXE maps (Fig. 8b), the pixels enclosed by a white dashed polygon have been selected for elemental quantification, as they exhibit the highest abundances of S and the lower abundance of contaminants elements.

With regard to the estimation of element concentration in the analysed areas of pyrite, Table 2 presents the μ-PIXE results for the three crystals that were analysed in their original state, without prior treatment with laser micro-ablation, and the ten crystals that were treated in accordance with the new workflow. The results presented here show only the major components of pyrite (S and Fe), together with the main contaminants. The full set of elemental quantification results can be found in Table 1S of the Online Resource 2. The values of the contents of Ni and Cu, which are relevant for the provenance discrimination, are shown in Fig. 9 for non-treated crystals (a) and for the treated ones (b), directly in comparison with the correspondent values from the Afghan, Tajik and Myanmar rocks reference dataset.

Although the comparison is not made between the same crystals, Table 1 provides the first quantitative evidence of the effects of the laser micro-ablation on altered pyrites. The S content increases significantly from values < 4 wt% to values between 23 and

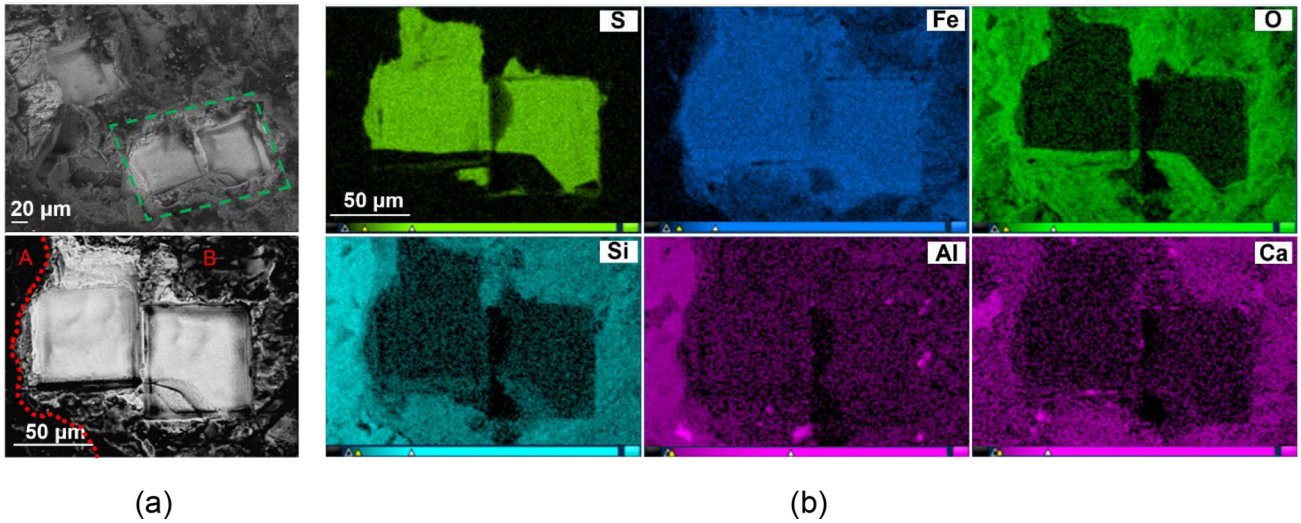

Fig. 7 **a** SEM-BSE image of a micro-ablated pyrite in T2 bead, three squared areas were irradiated (top). A zoom on the area highlighted by the dashed green box is visible in the bottom image. The red dashed line divides area A, where another mineral phase is present, from area B, where there is the pyrite (altered and pristine). **b** SEM–EDX elemental maps corresponding to the dashed green box in **a**

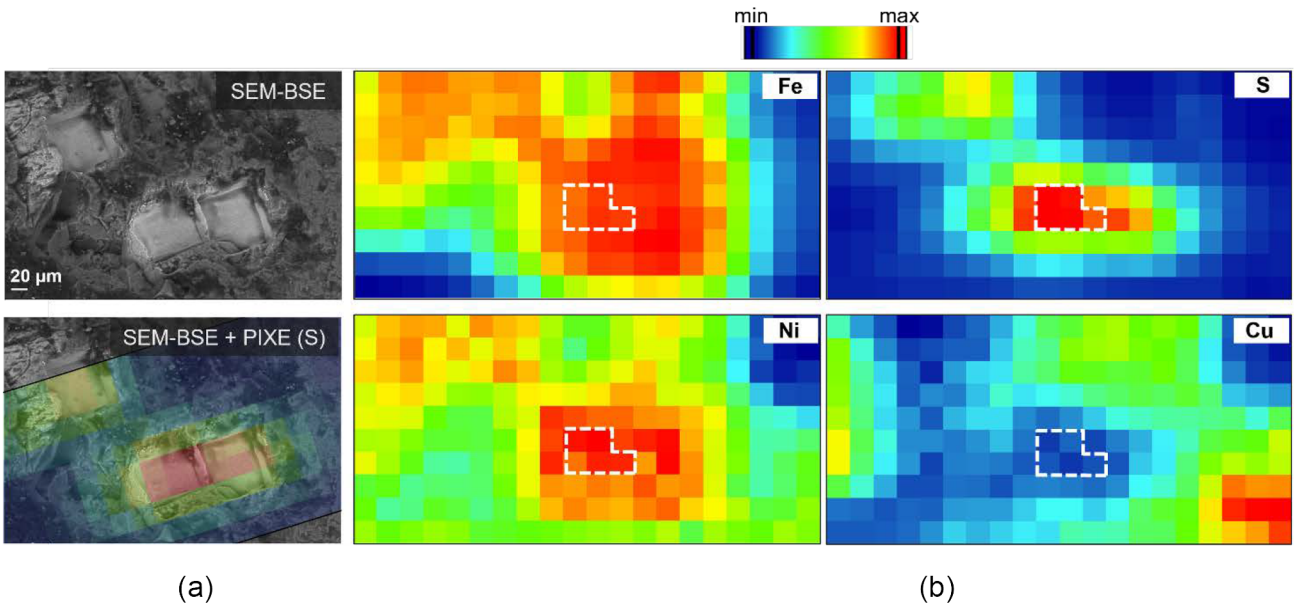

Fig. 8 **a** SEM-BSE image of the area containing the laser micro-ablated pyrite (top), and the same image overlapped the µ-PIXE map of sulphur (bottom): the appearance of S in the micro-ablated areas is evident. **b** µ-PIXE maps of iron, sulphur, nickel and copper surrounding the area of the ablated pyrite (PIXE map dimension $500 \times 250\ \mu m^2$, pixel dimension $25 \times 25\ \mu m^2$). The white dashed polygon in the centre of the µ-PIXE maps defines the area containing the pixels selected for quantitative analysis

38 wt% in the areas treated with laser micro-ablation. The Fe content also increases by an average of 10 wt%. With regard to the main contaminating elements present in the alteration crust (Mg, Al, Si, K and Ca), it is possible to observe a general decrease in their concentration from a few wt% points to almost 10 wt% on average in the case of silicon. These values suggest that after laser micro-ablation treatment, the areas are more relatable to pristine pyrite, although there are still some differences with the expected stoichiometric values. As reported in [29], an ideal pyrite is expected to have a Fe content of 46.55 wt% while S is 53.45 wt%; some variability of these elements is expected in natural pyrites which also contain small amounts of other minor and trace elements as discussed in [30]. While the Fe contents measured in the analysed areas are similar to those expected (with values both above and below the stoichiometric estimate, but always with differences <6 wt%), the S contents are always underestimated by about 15–19 wt%. A possible explanation could be related to the measurement condition of the µ-PIXE itself: the cleaned square area has a side length of 65 µm, which is slightly larger than the beam size (40 µm). Consequently, if the initial position of the scan is not perfectly aligned with the cleaned area, it is plausible that the signal recorded in the associated pixels partially contains the contribution of the surrounding regions where the alteration crust is still present. This also would explain the presence of some contaminating

Table 2 [Not ablated]-Quantitative results for μ-PIXE analysis on 3 pyrite crystals in the Ur beads analysed as such, without laser micro-ablation treatment. [Ablated]-Quantitative results for μ-PIXE analysis on 10 pyrite crystals in the Ur beads analysed after the laser micro-ablation treatment. Concentration values and associated errors are reported in %wt

	Sample	Area	S conc ± err (%wt)	Fe conc ± err (%wt)	Mg conc ± err (%wt)	Al conc ± err (%wt)	Si conc ± err (%wt)	K conc ± err (%wt)	Ca conc ± err (%wt)
Not ablated	L	P1	3.4 ± 0.2	29.1 ± 0.4	3.5 ± 0.3	5.1 ± 0.3	17.1 ± 0.3	0.98 ± 0.04	3.8 ± 0.1
	L	P2	3.3 ± 0.2	36.9 ± 0.4	2.7 ± 0.3	3.2 ± 0.2	17.3 ± 0.4	0.83 ± 0.03	4.2 ± 0.1
	T1	P1	0.9 ± 0.1	38.0 ± 0.3	3.6 ± 0.2	2.1 ± 0.1	12.7 ± 0.2	1.13 ± 0.02	6.5 ± 0.1
Ablated	L	P1	27.0 ± 0.5	49.6 ± 0.1	1.8 ± 0.2	1.9 ± 0.2	4.2 ± 0.2	0.74 ± 0.02	2.3 ± 0.1
	L	P2	32.7 ± 0.5	49.9 ± 0.1	0.9 ± 0.2	0.9 ± 0.2	3.7 ± 0.2	0.35 ± 0.02	2.0 ± 0.1
	L	P3	24.2 ± 0.4	40.6 ± 0.1	1.7 ± 0.2	2.2 ± 0.2	7.5 ± 0.2	0.57 ± 0.02	3.7 ± 0.1
	T1	P1	24.1 ± 0.4	40.9 ± 0.4	1.6 ± 0.2	3.2 ± 0.2	7.1 ± 0.2	0.81 ± 0.02	3.5 ± 0.1
	T1	P2	30.7 ± 0.6	44.5 ± 0.5	1.1 ± 0.2	1.1 ± 0.1	5.6 ± 0.2	0.62 ± 0.02	2.8 ± 0.1
	T1	P3	36.0 ± 0.6	42.9 ± 0.5	1.1 ± 0.2	3.4 ± 0.2	3.1 ± 0.2	1.00 ± 0.03	1.7 ± 0.1
	T2	P1	37.9 ± 0.4	42.9 ± 0.4	0.8 ± 0.1	1.6 ± 0.1	4.3 ± 0.1	0.36 ± 0.01	1.6 ± 0.1
	T2	P2	26.5 ± 0.5	44.4 ± 0.5	2.4 ± 0.2	1.2 ± 0.1	6.6 ± 0.2	0.96 ± 0.02	2.4 ± 0.1
	T2	P3	29.4 ± 0.4	51.3 ± 0.6	0.8 ± 0.2	0.9 ± 0.1	4.3 ± 0.2	0.49 ± 0.01	1.7 ± 0.1
	T2	P4	27.6 ± 0.8	47.9 ± 0.9	1.1 ± 0.3	1.4 ± 0.3	5.8 ± 0.4	0.94 ± 0.03	1.8 ± 0.2

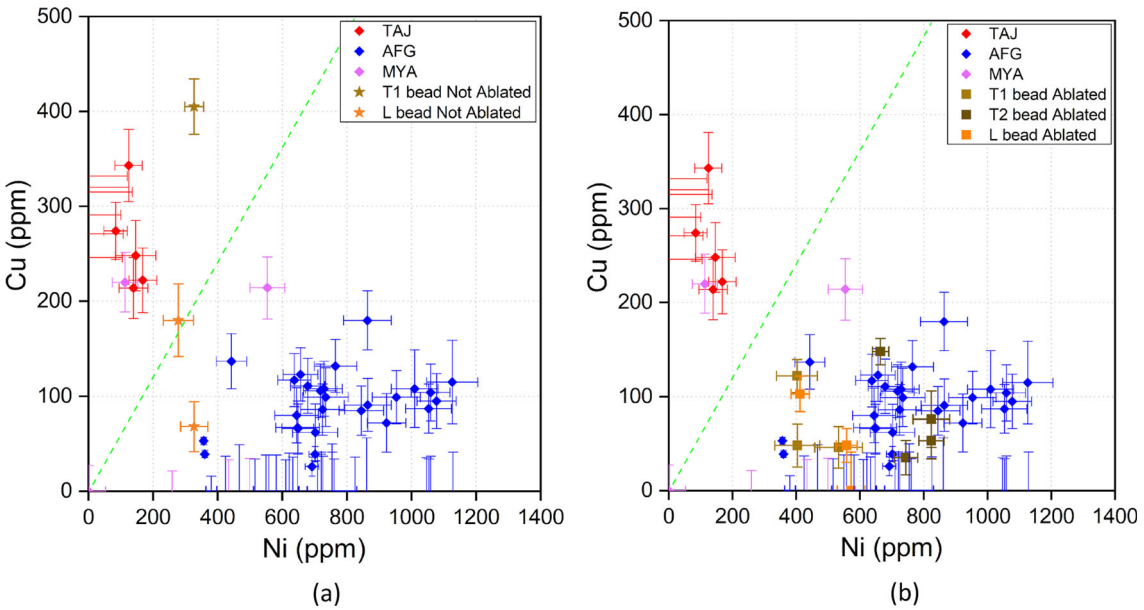

Fig. 9 Cu versus Ni trace element contents in pyrite: Graph (**a**) refers to μ-PIXE results of pyrites in Ur beads not treated with laser micro-ablation therefore analysed as such. Graph (**b**) refers instead to pyrites in Ur beads treated with laser micro-ablation, so after the alteration removal. The results are compared to data of reference rocks from Tajikistan (TAJ), Afghanistan (AFG) and Myanmar (MYA). The green dashed line defines the ideal separation between Tajikistan and Afghanistan data adopted in [9]

elements in concentrations of a few wt% points, whereas their signal was practically absent in the SEM–EDX spectra acquired on the same spots. The SEM–EDX probe has a smaller beam size and thanks to the BSE images it is also easier to identify the target area; however, the instrument available, working in variable pressure, does not allow the quantification of the elements of interest for direct comparison with the μ-PIXE results. Potential future enhancements to the methodology could involve a slight increase in the size of the cleaned area or the utilisation of smaller proton in-air beams (although this would entail a reduction in the current and an increase in measurement time).

Nevertheless, the application of the ablation treatment proved to be very significant in the evaluation of the Cu-Ni ratio and the relative provenance attribution considerations. As shown in Fig. 9a, altered pyrites would have suggested the exclusion of the Afghan provenance for the T1 bead and an indeterminate state for the L bead, with one point compatible with all the three reference datasets. In general, the cleaned areas (square points) are characterised instead by a reduction in Cu content and an increase in Ni

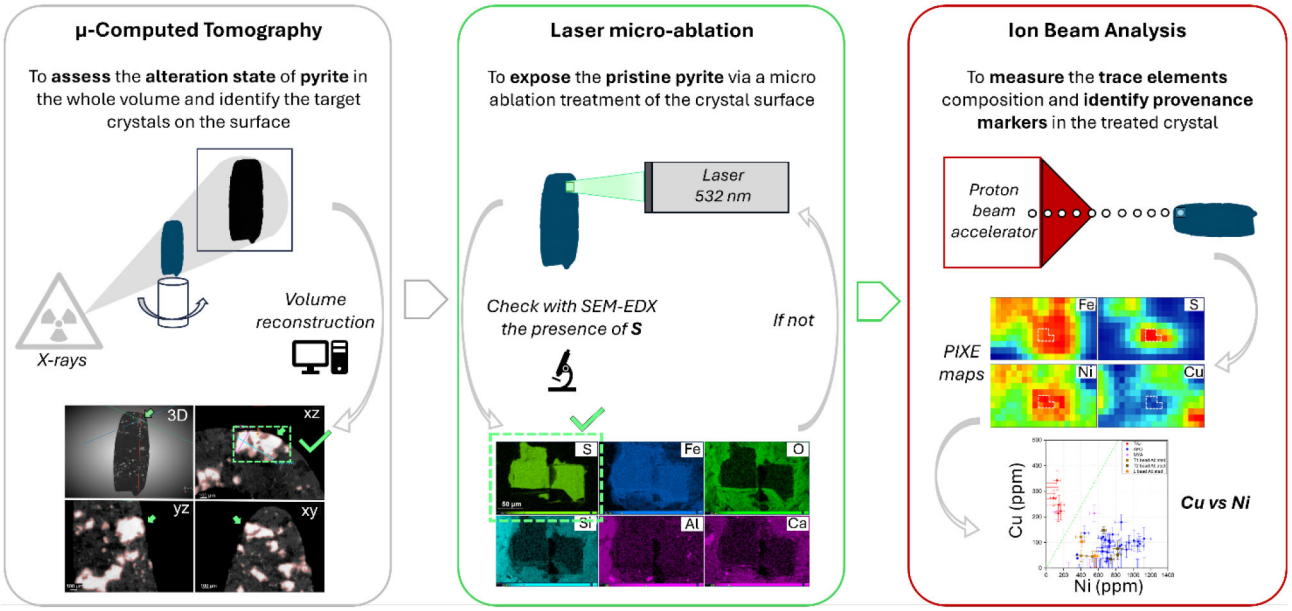

Fig. 10 Scheme of the steps that make up the proposed workflow applied to a lapis lazuli archaeological sample

content. As a result, all the points from the micro-ablated pyrites group clearly below the the Cu < 0.6·Ni threshold, leading for the three beads to the exclusion of the Tajik provenance according to [9], and leaving only an indeterminacy between Afghanistan and Myanmar provenance that cannot be discriminated using only pyrites. Looking at the representative example of the Ni and Cu maps in Fig. 8, in the areas treated with laser micro-ablation, the Ni distribution does not change significantly, and it reflects the Fe distribution, as also expected from the fact that in pyrite Ni^{2+} ions can stoichiometrically substitute Fe^{2+} ions in the lattice [30]. Instead, the Cu distribution appears to reflect the geometry of the micro-ablation, resulting in a lower abundance in the areas where S occurs compared to the surrounding altered areas. This is a major contributor to the shifting of the points of ablated pyrites in the Ni-Cu plot. It is important to note that, if the hypothesis of the collection of contaminating signals from the surroundings region is accepted, the Cu values displayed in the graph would be overestimated. Consequently, the true position of the points would be even further from the Cu < 0.6·Ni line towards the Afghan points. As discussed in [30], the presence of the Cu in pyrite may be related to the presence of microscopic inclusions of Cu-bearing mineral phases, but quantities of Cu may also be present in the pyrite lattice, especially in As-rich pyrites [31]. How the complex mechanism of alteration of pyrite then specifically affects the Cu content has not been investigated in the literature, at the best of our knowledge, but these first results clearly highlight the need for a removal of the alteration in order to have a reliable assessment of the provenance markers.

To summarise the procedure of the new developed workflow applied to an archaeological sample, a graphic representation of the different steps adopted is shown in Fig. 10.

4.2.2 Application of the provenance protocol

The data obtained from pyrite through the application of the new workflow can be integrated with the characterisation of other mineral phases, enabling the comprehensive application of the provenance protocol described in [9]. By the comparison with a large set of reference rocks from Chile, Siberia, Afghanistan, Tajikistan and Myanmar, it is possible to assess the origin of the raw material of the examined samples. In this work, seven additional reference samples from the Sar-i-Sang mines in Afghanistan are integrated for the first time with the overall dataset, leading to a total of 67 reference rocks. The extension of the database is a crucial activity that we pursue continuously in parallel whenever we are provided with lapis lazuli rocks of known origin. With the addition of new samples, some elemental concentration ranges will modify slightly compared to those presented in [9] and [32], but without changing the underlying methodology. Only one provenance marker threshold needs to be updated, and it will be indicated in its relevant protocol step. All the μ-PIXE data acquired from diopside and pyrite in the reference rocks are available in this open access repository on *Zenodo* platform [33, 34].

The initial step is to investigate the luminescence properties of the minerals forming the beads. The cold-CL technique was employed to map all the surfaces of the beads, with an illustrative example provided in Fig. 11. In all the samples, a dominant yellow luminescence typical of diopside crystals is observed, together with diffused dark areas related to non-luminescent phases, such as pyrite. No other luminescence phase seems to be present (e.g. calcite, K-feldspar and phlogopite). μ-PIXE and μ-IBIL analyses definitively confirmed the nature of the diopside. Nine diopside crystals were analysed in both L1 and T1 beads, while seven crystals in the T2 bead. Figure 12 shows two representative μ-IBIL spectra for each bead, acquired from different diopside crystals. The

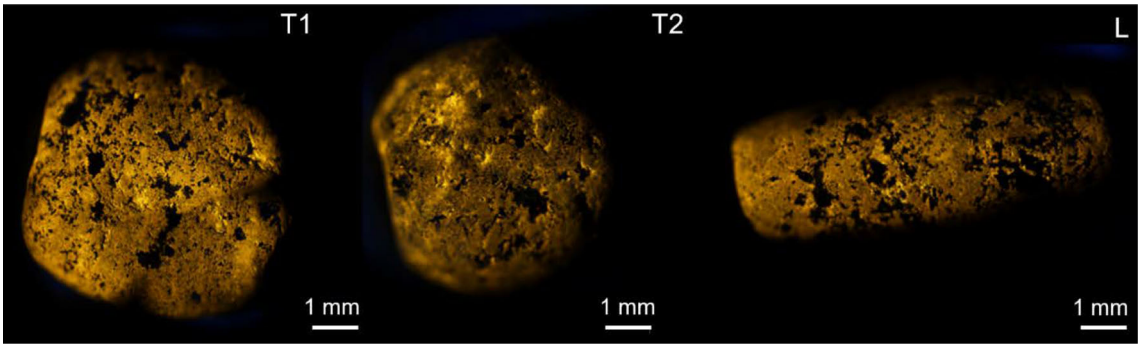

Fig. 11 Cold-CL images of the 3 lapis lazuli beads from Ur

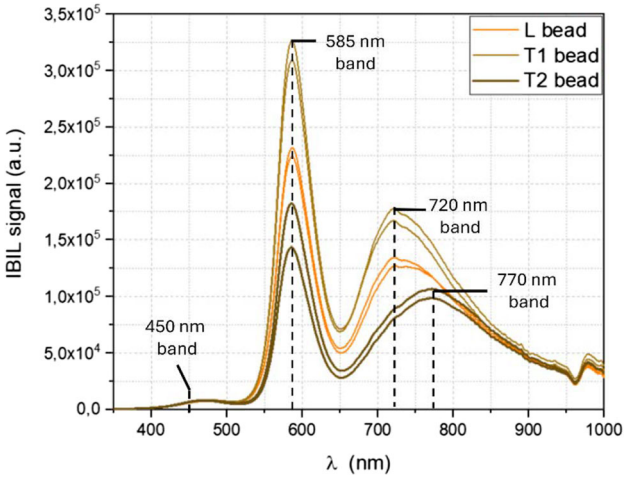

Fig. 12 Two representative μ-IBIL spectra of diopside crystals for each bead from Ur measured at New AGLAE. The position of the principal bands in diopside is marked with a label. T2 bead shows a characteristic band at 770 nm useful for provenance determination

spectra exhibit a primary peak at 585 nm, a broad band at approximately 450 nm [35], and, in the case of T2 bead, a broad band centred at 770 nm (for a review of the main activators of the bands see [35, 36]). In contrast, the secondary band observed in T1 and L beads appears to be more centred at 720 nm. In the protocol, the 770 nm band is a weaker marker for the Afghan provenance, providing an initial clue of the origin of the T2 raw material. The predominance of diopside with respect to wollastonite mineral phase is characteristic of Asian lapis lazuli rocks compared to Chilean rocks. In accordance with the archaeological context, the hypothesis of Chilean provenance can thus be rejected for all the beads.

In the second step of the protocol, the pyrite alteration state is evaluated together with the Sr content in diopside. As already mentioned in Sect. 2, a strong marker for the Siberian origin is the presence of pyrite crystals in a fully altered state, even in the innermost parts of the rock. As discussed in Sect. 4.2.1, the μ-CT of the Ur beads clearly revealed that pyrites in these samples were only superficially altered. This finding lends strong support to the exclusion also of a Siberian origin with good confidence. Further confirmation is provided by the evaluation of Sr concentrations in diopside (Fig. 13): all the values found in the crystals of the Ur beads, with the exception of one point in T2 (320±30 ppm), are below the threshold of 234 ppm, which is a weaker marker for Siberia origin. In the present study, this threshold was updated by considering one sigma above the new maximum Sr content for the Afghan dataset (200±40 ppm) found through the database extension.

The laser micro-ablation treatment on pyrite crystals allowed to complete the third step of the protocol, namely the evaluation of the Cu and Ni content ratio to possibly exclude the Afghan or the Tajikistan origin (since Myanmar rocks are not discriminated by these factors). As illustrated in Fig. 9b, the results of Ur beads are fully compatible with the Afghan–Myanmar region of the graph, allowing to reject the hypothesis of a Tajik origin of the material for all the beads. The final stage of the protocol involves the evaluation of trace element concentrations in diopside. Figure 13 shows the μ-PIXE results for the most relevant elements in the provenance discrimination; the comprehensive results for the Ur beads are presented in Table 2S of the Online Resource 2. The box plots illustrate the dispersion of the experimental points (0.25–0.75 percentile values) for each bead and each reference geological dataset; error bars are not reported to enhance the clarity of the graphs. The median line and the minimum and maximum values are indicated. The symbols represented by squares at the value of zero indicate the number of measurements that fell below the limits of detection (LOD).

The three Ur beads display a relatively high concentration of Ti, Mn and Cr in diopside. Considering the thresholds delineated in the protocol as Afghan weaker markers (Ti > 800 ppm, Mn > 310 ppm and Cr > 75 ppm), it can be observed that all the crystals exhibit Ti and Mn values fulfilling these conditions. Conversely, for Cr, eight out of nine points in L, seven out of nine points in

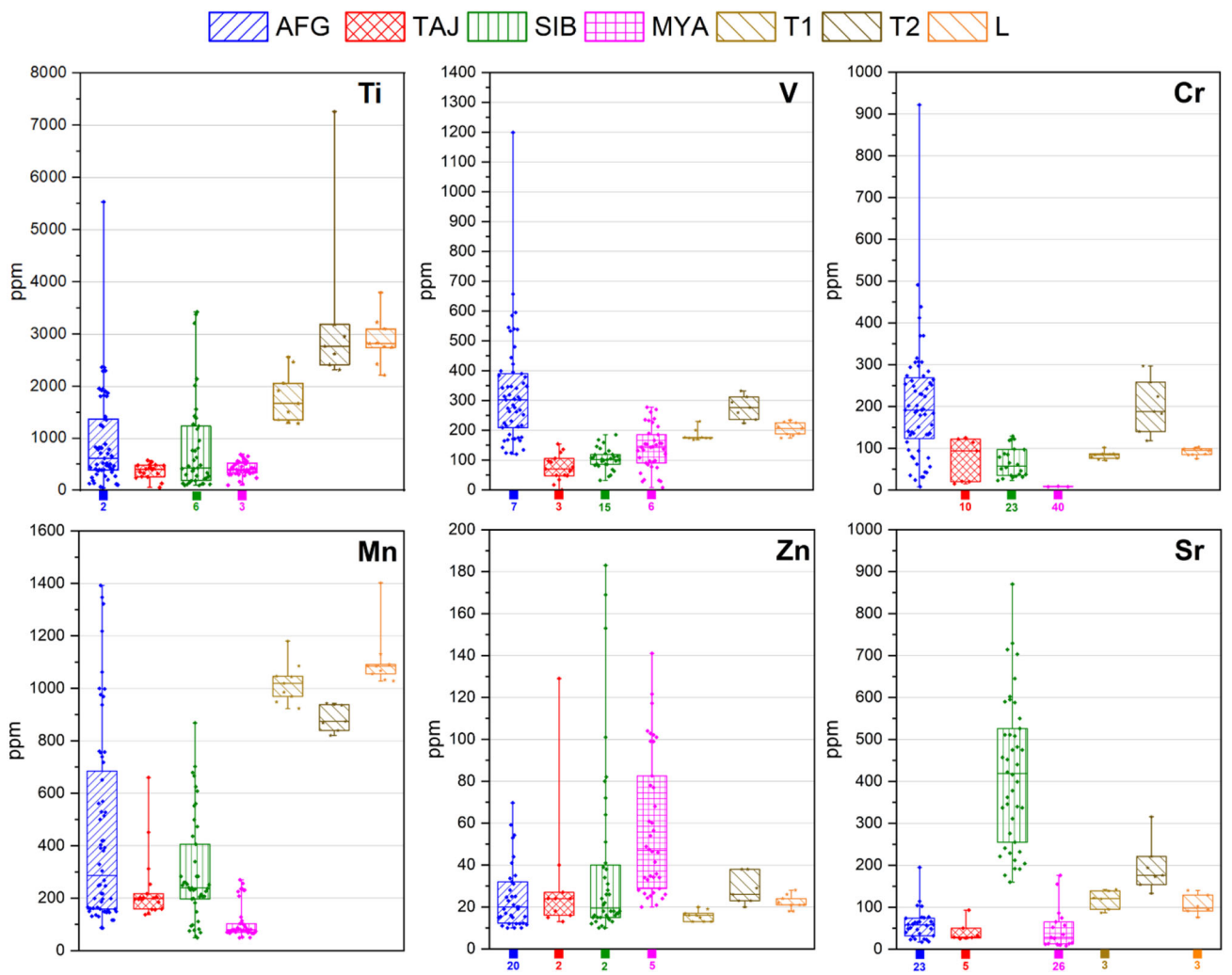

Fig. 13 μ-PIXE results for trace elements concentration in diopside, comparing results from Ur beads to data from the reference geological samples, grouped by provenance area. The box plots represent the dispersion of the experimental points: the median line and the two percentile values 0.25 and 0.75. The squared symbols in correspondence to 0 value represent the number of measurements below the limit of detection (LOD)

T1 and seven out of seven points in T2 exceed the corresponding threshold. In a single instance, the vanadium Afghan marker (V > 320 ppm) is also present (330 ± 30 ppm in T2 bead); the V concentration in all the other crystals is consistent with the Afghan range. Furthermore, the Zn content is also compatible with the Afghan dataset for all the beads, and it is found to be below the threshold of 77 ppm that was identified as a Myanmar weaker marker in [32] (the maximum Zn found is 38 ± 6 ppm in the T2 bead). To summarise, the results obtained from μ-PIXE and μ-IBIL analysis of both pyrite and diopside mineral phases indicate that the Afghan provenance, among those considered in this study, is the most probable source of the raw materials used for the carving of the three beads discovered at Ur.

The attribution to the Afghan quarry district obtained by the combination of the new workflow with the markers of the provenance protocol can be cross validated by the application of Principal Component Analysis to diopside data. As described in detail in [37], this multivariate approach has proved to be very effective in enhancing the role of Cr, Ti, V and Mn and their correlation for the discrimination of the Afghan provenance. An example of application to this method to lapis lazuli archaeological beads is discussed in [32]. A custom-made Python script (developed in Spyder 3.3.1 scientific environment) was employed for the PCA calculation and graph representation. The variables considered are the elements identified as diopside weaker markers in the protocol. Figure 14 shows the Principal Component 2 (PC2) versus PC1 biplot obtained from the μ-PIXE diopside data of reference rocks of the database, including the new samples added. Score values, calculated from the data of Ur beads, are plotted on the same space of this biplot after a scaling procedure using the same mean and standard deviation as the database model. The colour differentiation according to the provenance is applied only in the plotting procedure, and it does not influence the score values. Concerning the results of the three Ur beads, it is possible to see that the data of all the beads group well together in the biplot thanks to a similar contribution to PC1 and PC2. The outlier point of T2 is the crystal characterised by the highest content of Ti that emerged also in Fig. 13. This

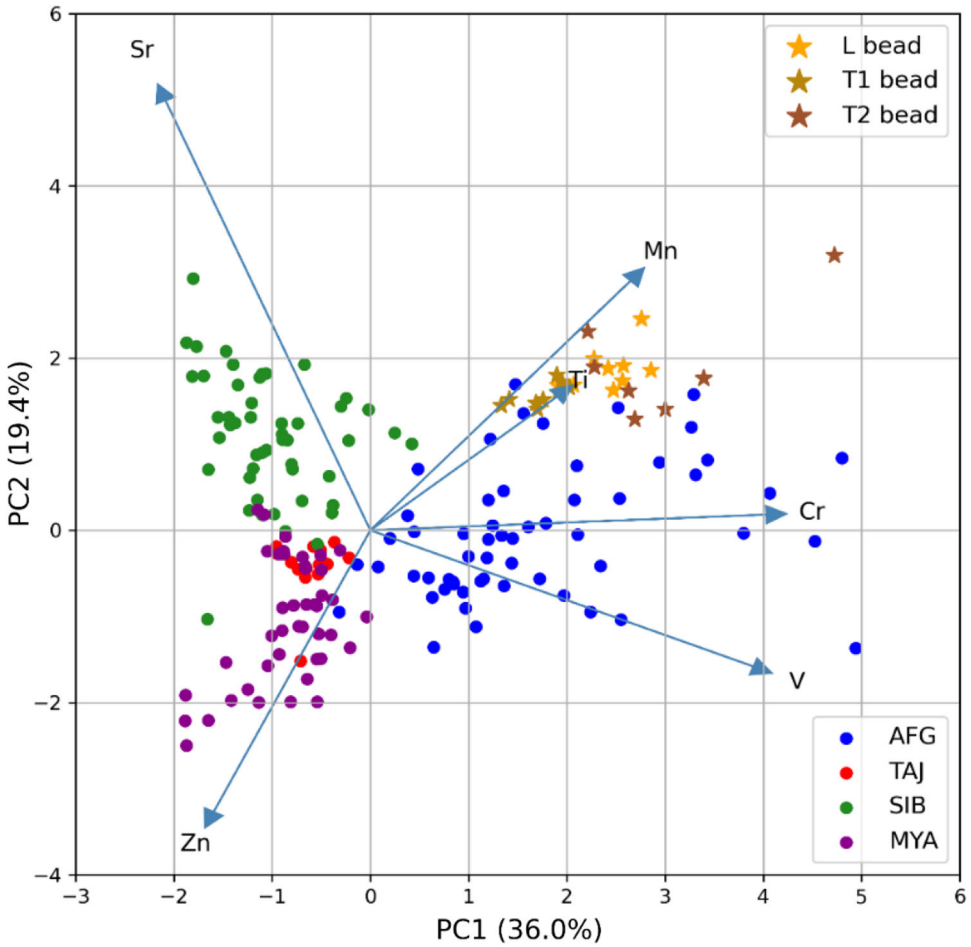

Fig. 14 PC2 versus PC1 biplot obtained from PCA analysis on μ-PIXE data acquired on diopside crystals from all geological reference samples. μ-PIXE data for trace elements in diopside from Ur beads are projected on the PCs space. The percentage of explained variance for each PC is reported in brackets

approach demonstrates, once again, that the Ur beads exhibit the highest degree of compatibility with the Afghan dataset. The graph of PC1 versus PC3 with the projection or the Ur data is reported in Online Resource 3 and shows similar compatibility. The first three principal components cover the 71% of the variability of the dataset.

5 Conclusion

This paper presents a novel methodology based on the characterisation of pyrite crystals to support the investigation of the lapis lazuli provenance. The workflow developed employs a micro-invasive approach, and it is particularly suited to cases of valuable archaeological samples exhibiting surface degradation processes affecting the pyrite mineral phase. Several different techniques were utilised: X-ray micro-computed tomography, laser micro-ablation and ion beam analysis. μ-CT has proved to be extremely effective in assessing the alteration state of pyrite crystals within the entire volume of the lapis lazuli rock, providing for the first time a non-invasive method to potentially confirm or exclude the Siberian origin of the rock. In cases where the pyrite crystals exhibit only a surface crust of alteration, μ-CT can also be used as a guideline for selecting the most suitable crystals for subsequent laser micro-ablation. The micro-ablation procedure presented in this study succeeded in removing the alteration crust and exposing the underlying preserved crystal, facilitating a more significant analysis of its elemental composition using IBA. Indeed, an accurate assessment of the Ni and Cu trace elements in pyrite can provide crucial insights into the origin of the material, distinguishing between Afghan and Tajik provenance.

Furthermore, this study presents the first application of the workflow to archaeological lapis lazuli material exhibiting severe degradation of pyrites. The results demonstrated the efficacy of integrating this new methodology with a previously validated provenance protocol, which was applicable in its full version only in the case of perfectly conserved samples. Three lapis lazuli beads from the Royal Graves at Ur of the Chaldees, in southern Mesopotamia (Iraq, 3rd millennium BCE) were analysed. Despite the long-standing assumption that the vast quantities of lapis lazuli found in Ur had been sourced from the distant region of Badakhshan in North–east Afghanistan, this hypothesis remained unproven at the scientific level. An analytical comparison of the physical–chemical characteristics of the material with a dataset of reference rocks from Chile, Tajikistan, Myanmar, Siberia and Afghanistan enabled

this study to prove, for the first time with a non-destructive method, that lapis lazuli beads from Ur are compatible with rocks extracted from the Afghan mines. The importance of this discovery cannot be overestimated, as analytical clues have finally been provided indicating that the lapis lazuli found in this archaeological context most likely came from Afghanistan. This outcome makes it possible to follow the changing fortunes of this remarkable long-distance trade, one of the earliest, which began as early as the 5th millennium BCE and still continues to the present day.

Supplementary Information The online version contains supplementary material available at https://doi.org/10.1140/epjp/s13360-025-05988-9.

Acknowledgements The authors wish to warmly thank IPERION HS (Grant Agreement n. 871034) EU Transnational Access programme for the financial support of SIBILLA and LATERAL projects. The *GFI: Grant For Internationalisation* promoted by the Physics Department of the University of Torino is also acknowledged for the financial support. The EQUIPEX NEW AGLAE research programme (n. ANR-10-EQPX-22, French Ministry of Research) is acknowledged. The authors wish to thank Prof. Luca Martire for the availability of the Cold-CL apparatus, and the scientific laboratories of the Centro Conservazione e Restauro "La Venaria Reale", Torino (Italy), for the SEM instrumentations. Mr. Guy Clutterbuck is greatly acknowledged for his precious help in providing us reference rock samples from Afghanistan.

Funding Open access funding provided by Università degli Studi di Torino within the CRUI-CARE Agreement.

Data availability Statement All relevant data generated or analysed during this study are included in this manuscript or available at Zenodo public repositories as indicated; additional information can be granted upon reasonable request to the authors. The manuscript has data included as electronic supplementary material.

Declarations

Conflict of interest The authors have no affiliations with or involvement in any organisation or entity with any financial interest or non-financial interest in the subject matter or materials discussed in this manuscript.

References

1. G. Hermann, Iraq **30**(1), 21–57 (1968). https://doi.org/10.2307/4199836
2. G. Hermann, P.R.S. Moorey, Lapis Lazuli, in *Reallexikon der Assyriologie und Vorderasiatischen Archäologie*. ed. by E. Ebeling (De Gruyter, Berlin, 1938), pp.489–492
3. M. Casanova. Le lapis-lazuli dans l'Orient Ancien: production et circulation du Néolithique au IIe millénaire av. J.-C. (Editions du Comité des travaux historiques et scientifiques, Paris, 2013).
4. A.B. Delmas, M. Casanova, South Asian Archaeol. **9**, 393–426 (1987)
5. S. Ratnagar, Curr. Anthropol. **42**(3), 351–379 (2001). https://doi.org/10.1086/320473
6. D.D. Hogarth, W.L. Griffin, Lithos **11**, 37–60m (1978). https://doi.org/10.1016/0024-4937(78)90030-0
7. D. Angelici, Petrographic and minero-chemical characterisation of lapis lazuli: a provenance study of rocks and artefacts from Cultural Heritage, PhD thesis, Università degli Studi di Torino (2015).
8. A. Lo Giudice, D. Angelici, A. Re, G. Gariani, A. Borghi, S. Calusi, L. Giuntini, M. Massi, L. Castelli, F. Taccetti, T. Calligaro, C. Pacheco, Q. Lemasson, L. Pichon, B. Moignard, G. Pratesi, M.C. Guidotti, Archaeol. Anthropol. Sci. **9**(4), 637 (2017). https://doi.org/10.1007/s12520-016-0430-0
9. L. Guidorzi, A. Re, M. Magalini, D. Angelici, A. Borghi, G. Vaggelli, F. Fantino, V. Rigato, L. La Torre, Q. Lemasson, C. Pacheco, L. Pichon, B. Moignard, A. Lo Giudice, Eur. Phys. J. Plus **138**(2), 175 (2023). https://doi.org/10.1140/epjp/s13360-023-03768-x
10. T. Calligaro, Y. Coquinot, L. Pichon, G. Pierrat-Bonnefois, P. De Campos, A. Re, D. Angelici, Nucl. Instrum. Method. Phys. Res. B **318**, 139–144 (2014). https://doi.org/10.1016/j.nimb.2013.06.063
11. J.D. Rimstidt, D.J. Vaughan, Geochim. Cosmochim. Acta **67**(5), 873–880 (2003). https://doi.org/10.1016/S0016-7037(02)01165-1
12. A. Re, D. Angelici, A. Lo Giudice, E. Maupas, L. Giuntini, S. Calusi, N. Gelli, M. Massi, A. Borghi, L.M. Gallo, G. Pratesi, P.A. Mandò, Appl. Phys. A Mater. Sci. Process. **111**(1), 69 (2013). https://doi.org/10.1007/s00339-013-7597-34
13. M. Schreiner, M. Strlič, R. Salimbeni, *Handbook on the use of lasers in conservation and conservation science* (COST G7 Publisher: COST office, Brussels, 2008)
14. M. Bertasa, C. Korenberg, J. Cult. Herit. **53**, 100–117 (2022). https://doi.org/10.1016/j.culher.2021.10.010
15. M. Abraham, P. Northover, G. Grime, J. Cult. Herit. **1**, S317–S324 (2000). https://doi.org/10.1016/S1296-2074(00)00154-0
16. C. L. Woolley, The Royal Cemetery, Ur Excavations, Volume II (hereafter U.E. II). Ublications of the joint expedition of the British Museum and of the museum of the University Of Pennsylvania to Mesopotamia (1934).
17. A. Mazzinghi et al., Eur. Phys. J. Plus **139**, 635 (2024). https://doi.org/10.1140/epjp/s13360-024-05429-z
18. D.R. Baker, L. Mancini, M. Polacci, M.D. Higgins, G.A.R. Gualda, R.J. Hill, M.L. Rivers, Lithos **148**, 262–276 (2012). https://doi.org/10.1016/j.lithos.2012.06.008
19. V. Cnudde, M.N. Boone, Earth Sci. Rev. **123**, 1–17 (2013). https://doi.org/10.1016/j.earscirev.2013.04.003
20. L. Vigorelli, E. Croce, D. Angelici, R. Navone, S. Grassini, L. Guidorzi, A. Re, A. Lo Giudice, Condens. Matter **6**(4), 51 (2021). https://doi.org/10.3390/condmat6040051
21. H. Alarashi, M. Benz, J. Gresky, A. Burkhardt, A. Fischer, L. Gourichon, M. Gerlitzki, M. Manfred, J. Sakalauskaite, B. Demarchi, M. Mackie, PLoS ONE **18**(8), e0288075 (2023). https://doi.org/10.1371/journal.pone.0288075

22. D. Nykonenko, O. Yatsuk, L. Guidorzi, A. Lo Giudice, F. Tansella, L.P. Cesareo, G. Sorrentino, P. Davit, M. Gulmini, A. Re, Herit. Sci. **11**(1), 238 (2023). https://doi.org/10.1186/s40494-023-1078-0
23. R. Brancaccio, M. Bettuzzi, F. Casali, M.P. Morigi, G. Levi, A. Gallo et al., IEEE Trans. Nucl. Sci. **58**, 1864–1871 (2011). https://doi.org/10.1109/TNS.2011.2158850
24. C.A. Schneider, W.S. Rasband, K.W. Eliceiri, Nat. Methods **9**, 671–675 (2012). https://doi.org/10.1038/nmeth.2089
25. L. Pichon, B. Moignard, Q. Lemasson, C. Pacheco, P. Walter, Nucl. Instrum. Method. Phys. Res. Sect. Bm **318**(PART A), 27 (2014). https://doi.org/10.1016/j.nimb.2013.06.065
26. L. Pichon, T. Calligaro, V. Gonzalez, Q. Lemasson, B. Moignard, C. Pacheco, Nucl. Instrum. Method. Phys. Res. B **348**, 68 (2015). https://doi.org/10.1016/j.nimb.2015.01.010
27. L. Pichon, T. Calligaro, Q. Lemasson, B. Moignard, C. Pacheco, Nucl. Instrum. Method. Phys. Res. Sect. B **363**, 48 (2015). https://doi.org/10.1016/j.nimb.2015.08.086
28. R. Law, *My life is like the summer rose Maurizio Tosi e l'Archeologia come modo di vivere* (Archaeopress, Oxford, 2014), p.429
29. https://webmineral.com/data/Pyrite.shtml. Accessed 20 July 2024
30. P.K. Abraitis, R.A.D. Pattrickand, D.J. Vaughan, Int. J. Miner. Process. **74**(1–4), 41–59 (2004). https://doi.org/10.1016/j.minpro.2003.09.002
31. M.T. Einaudi, Am. Miner. **53**(9–10), 1748–1752 (1968)
32. M. Magalini, L. Guidorzi, A. Re, D. Frenez, K.D. Williams, K.A. Douglas, N.S. al-Jahwari, Q. Lemasson, C. Pacheco, L. Pichon, B. Moignard, A. Lo Giudice. First provenance evidence for lapis lazuli artefacts from Arabia: Analytical study of beads from the Umm an-Nar tomb DH7-1 at Dahwa, Sultanate of Oman. J. Archaeol. Sci. **174**, 106131 (2025). https://doi.org/10.1016/j.jas.2024.106131
33. A. Lo Giudice, A. Re, L. Guidorzi, M. Magalini. Database of elemental concentration of diopside in lapis lazuli rocks of different provenances obtained by micro-PIXE (2024). Zenodo. https://doi.org/10.5281/zenodo.14281286
34. A. Lo Giudice, A. Re, L. Guidorzi, M. Magalini. Database of elemental concentration of pyrite in lapis lazuli rocks of different provenances obtained by micro-PIXE (2024). Zenodo. https://doi.org/10.5281/zenodo.14281885
35. M. Gaft, R. Reisfeld, G. Panczer, *Modern Luminescence Spectroscopy of Minerals and Materials* (Springer Mineralogy, New York, 2015)
36. C.M. Macrae, N.C. Wilson, Luminescence database I—minerals and materials. Microsc. Microanal. **14**(2), 184–204 (2008). https://doi.org/10.1017/S143192760808029X
37. L. Guidorzi, A. Re, M. Magalini, A. Lo Giudice, Nucl. Instrum. Method. Phys. Res. Sect. B **540**, 45–50 (2023). https://doi.org/10.1016/j.nimb.2023.04.007